11-1-2014

Application of the Monopole Source to Quantify Explosive Flux During Vulcanian Explosions at Sakurajima Volcano (Japan)

Jeffrey B. Johnson
Boise State University

Alex J.C. Miller
Boise State University

Application of the Monopole Source to Quantify Explosive Flux during Vulcanian Explosions at Sakurajima Volcano (Japan)

by Jeffrey B. Johnson and Alex J. C. Miller

INTRODUCTION

A primary goal in volcano seismology is to characterize source motions internal to a volcano in terms of their representative forces. In a similar manner, much volcano infrasound research strives to recover eruptive force time histories corresponding to material accelerations occurring at Earth's free surface. These motions may correspond to explosive emission of gas and pyroclasts (e.g., Banister, 1984), rapid ground distensions of a volcanic dome (e.g., Johnson and Lees, 2010), and/or gravity driven rock fall or pyroclastic flows (e.g., Yamasato, 1997). When free surface motion is unsteady it imposes stresses upon the surrounding atmosphere, which are propagated as acoustic airwaves. Typically, the sounds produced by volcanic phenomena are recorded with low-frequency infrasound sensitive microphones. The intervening atmosphere is relatively homogeneous and nonattenuating for infrasound propagation of a few kilometers, therefore the recorded excess pressures closely represent volcano source time functions. Such force time histories are equivalent to volumetric accelerations of the atmosphere at or near to the source.

Many volcano explosion signals begin with intense, impulsive bipolar pulses (compression followed by rarefaction) with durations of a few seconds or less (e.g., Morrissey and Chouet, 1997). These volcano explosion waveforms are often similar to chemical explosion signals recorded in the far field and are suggestive of a rapid release and expansion of gases (Kitov *et al.*, 1997). Several volcano infrasound studies have made use of the Lighthill (1978) simple acoustic source to characterize ejection of fluid from the volcanic vent (e.g., Johnson, 2003).

THE SIMPLE ACOUSTIC SOURCE APPLIED TO VOLCANOES

Volcanic explosions generate bipolar infrasound pulses with durations of a few seconds (Firstov and Kravchenko, 1996; Johnson, 2003) that have been attributed to simple acoustic sources. A simple acoustic source, or a monopole, corresponds to a point approximation of fluid injection or extraction. Although most volcanic vents possess length scales of tens of meters to hundreds of meters the compact volcano source designation is reasonable for many strombolian or small vulcanian eruptions where principal acoustic radiation possesses wavelengths of hundreds of meters (Fee and Matoza, 2013). For example, Johnson *et al.* (2004), Johnson *et al.* (2008), and Gerst *et al.* (2013) used the monopole source to quantify explosive gas emissions at Mount Erebus (Antarctica). They inferred gas burst outfluxes from the 40 m diameter lake on the order of 10^3 m^3 during ~1 s eruptions. Considering that dominant infrasound frequencies were less than 2 Hz, they assumed a compact source geometry and invoked the Lighthill (1978) equivalence of the excess pressure δp to the displaced atmospheric mass rate of change.

$$\ddot{V}(t) = \frac{\ddot{M}(t)}{\rho_{\text{atmos}}} = \frac{2\pi r}{\rho_{\text{atmos}}}\delta p(t + r/c). \tag{1}$$

Here, the sound speed c affects the propagation time between source and receiver at distance r. The density ρ_{atmos} relates the mass acceleration $\ddot{M}$ of displaced atmosphere to the volume acceleration $\ddot{V}$ of the displaced medium. Hemispherical radiation is assumed, for which acoustic energy radiates outward with a solid angle of 2π.

From equation (1), a source volume flux may be inferred as the time integrated excess pressure:

$$\dot{V}(t) = \frac{2\pi r}{\rho_{\text{atmos}}}\int \delta p(t + r/c)dt. \tag{2}$$

Cumulative volume injection/ejection is the twice time integrated excess pressure record:

$$V(t) = \frac{2\pi r}{\rho_{\text{atmos}}}\int\left(\int \delta p(t + r/c)dt\right)dt. \tag{3}$$

This double integration of the excess pressure record is particularly sensitive to long-period pressure fluctuations of the volcano infrasound signal. Unfortunately, it is also highly sensitive to low-frequency noise or instrument drift artifacts. Significant flux and cumulative flux artifacts may also arise from digital filtering of the pressure signal, or from improper accounting of instrument response. These influences must be understood to properly recover estimates of explosive gas emissions.

doi: 10.1785/0220140058

EXPERIMENT OVERVIEW

This paper applies the monopole source model to vulcanian explosive eruptions at Sakurajima to recover flux and cumulative flux associated with perturbed atmosphere. We modify the double integration method used at Mount Erebus (e.g., Johnson *et al.*, 2004; Gerst *et al.*, 2013), and apply it to the considerably larger Sakurajima vulcanian explosions (see examples in Fig. 1). We then compare cumulative flux results to time-lapse image sequences to quantify expanding plume volumes. Scaling relationships between visual plume observations and infrasound modeling are discussed.

All data presented here was recorded between 19 and 21 July 2013 and comes from an infrasound array deployed for one week at the Kurakami Array Site (KURA), 3500 m from the active vent (Fig. 2; Fee *et al.*, 2014; this Focus Section). Global Positioning System (GPS) time stamped pressures signals were continuously recorded with 24-bit DataCube loggers at 200 Hz. Sensors were identical micro electro-mechanical systems-based infrasonic microphone (infraBSU) characterized by a single-pole corner at 26 s. The operation and response of this type of sensor is discussed in Marcillo *et al.* (2012). We use data from KURA station channels 1, 2, 4, and 6 because their recordings were cleanest in terms of wind noise. KURA sensors were located proximally to the volcano and with line-of-sight to the Showa Crater rim.

In the following section, we highlight a signal processing technique that is needed to robustly apply the monopole source model to the relatively long duration (10–25 s) Sakurajima eruption pulses. High-amplitude Sakurajima eruption infrasound, occurring as frequently as 10^3 times per year (since 2009; Yokoo *et al.*, 2013), is thought to be generated by swelling of the vent rock followed by the sudden release of pressurized gas pockets in the Showa Crater (Yokoo *et al.*, 2013). Characteristic signal signature is a few second long compression (spectral content is dominated by ~0.4 Hz energy) followed by a somewhat longer rarefaction often overprinted with a decaying oscillating sinusoid (refer to events I, V, VII, IX, and X in Fig. 1 for type examples). During the first few tens of seconds, array analyses confirms that most infrasound is directly propagated from the vent region, as opposed to infrasound that is later reflected off of distant topographic features (Yokoo *et al.*, 2014; this Focus Section).

FINITE WINDOW ZERO PRESSURE ZERO FLUX (FWZPZF) CORRECTION

In this section, we showcase the signal conditioning used to process a Sakurajima infrasound transient and convert it to time history of cumulative eruptive gas flux. We introduce and apply a signal correction technique that allows robust estimates of flux and cumulative flux out to several tens of seconds. Lacking this type of conditioning, derived monopole explosive volume flux estimates are limited to only a few seconds, as was the case for monopole studies at Erebus (e.g., Johnson *et al.*, 2004).

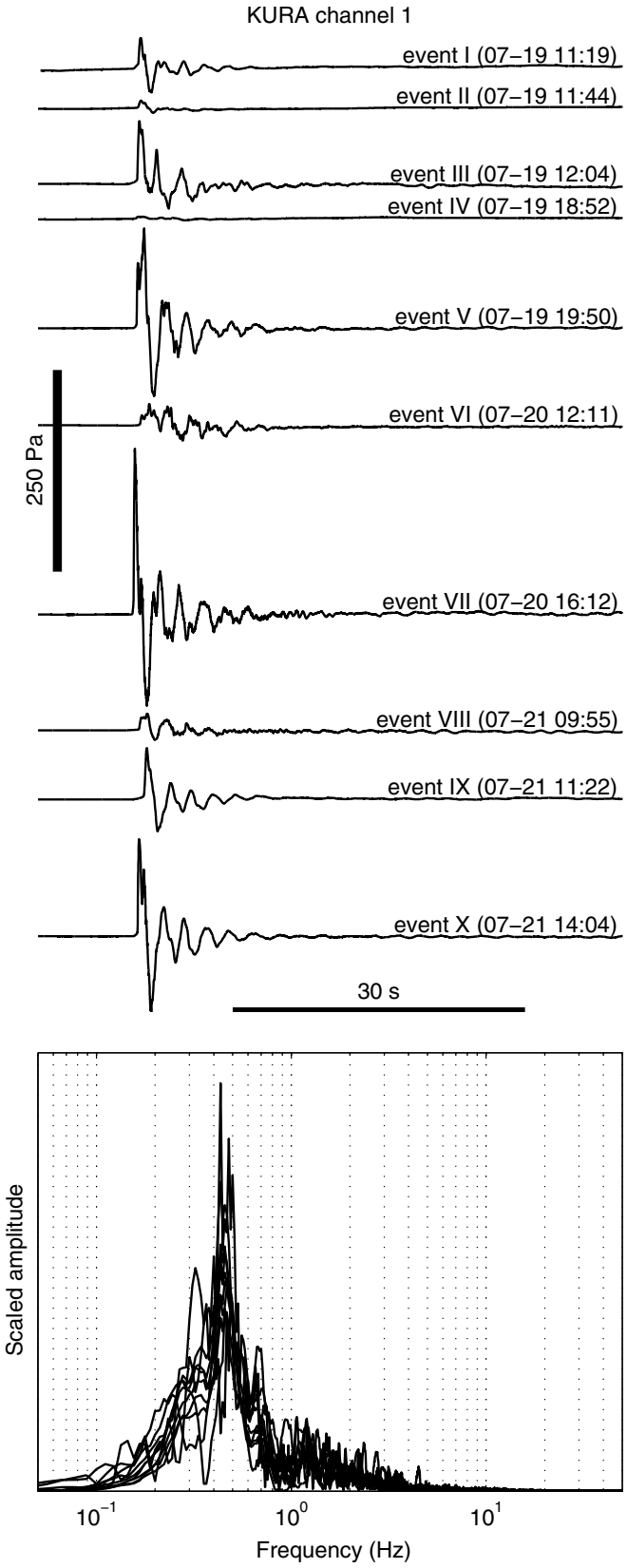

▲ **Figure 1.** (Top) Collection of the ten infrasound events recorded on channel 1 of the KURA array, ~3500 m from the vent. These signals comprise those events analyzed in this study. (Bottom) Normalized amplitude spectra for the ten different events filtered above 0.2 Hz.

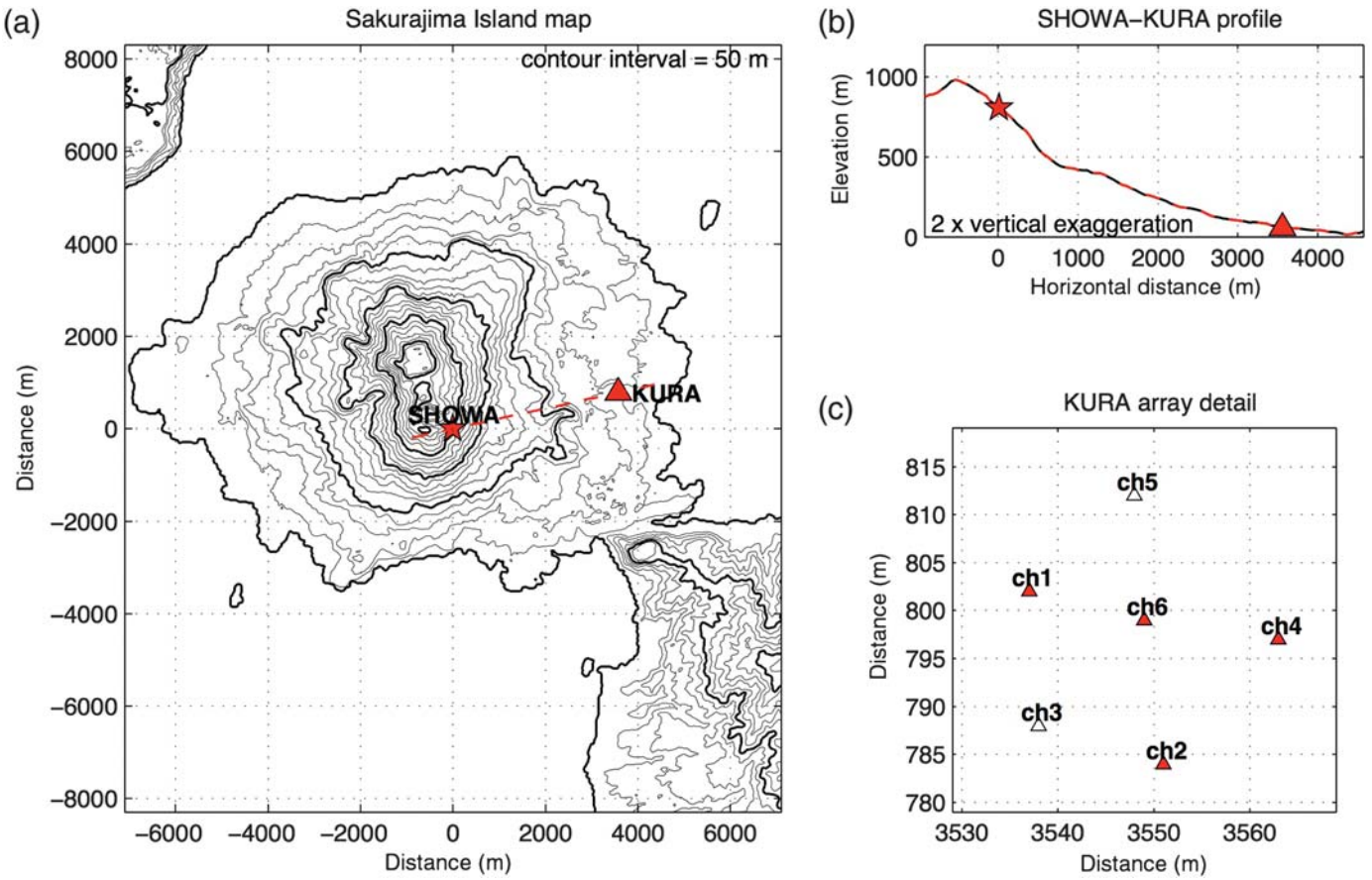

▲ **Figure 2.** (a) Map and (b) profile showing the location of the KURA infrasound array in relation to Sakurajima Volcano and the Showa Crater. (c) Detail of array indicating channels 1, 2, 4, and, 6 used in the analyses.

As an example, we use Sakurajima event number III (from Fig. 1), which is a relative large explosion that has a decent signal-to-noise ratio (see Table 1). It is important to note that this, and many other Sakurajima vulcanian eruption signals, possess high signal-to-noise owing to quiet deployment sites, relative proximity of receivers to the vent, and high-intensity acoustic sources. This makes Sakurajima signals excellent candidates for investigation of explosive outflux.

We begin by demonstrating the potential deleterious influence of noise and instrument drift, as well as filtering artifacts, on recovery of cumulative flux values. Noise is a component of infrasound recordings and is especially pronounced for longer periods (e.g., below 1 Hz). Even during quiet (windless) conditions raw infrasound records $\delta p_r(t)$ comprise a superposition of volcano signal and both electronic and ambient noise. Although ambient infrasound noise can be wide band, it is particularly pronounced at microbarom frequencies between 0.08 and 0.5 Hz (Bowman *et al.*, 2005; Matoza *et al.*, 2013), and has the potential to obscure long wavelength volcano infrasound signal. Instrument drift, arising from thermal influences, is also hard to avoid even with high fidelity sensors and temperature compensated electronics. In our experience, instrument noise is often manifested as a static offset or slowly drifting voltage over time scales of minutes to hours.

Event III from Sakurajima shows a typical good signal-to-noise explosive waveform recorded on channel 1 at KURA (Fig. 1), which was located ~3.5 km from the Showa Crater. The signal has been normalized in Figure 3 to draw attention to the effects of various filters and processing techniques. Equations (2) and (3) are applied to recover scaled volume fluxes (middle row of Fig. 3) and cumulative volume fluxes (bottom row) for a variety of processed signals, including (Fig. 3a) the mean-removed raw signal, (Fig. 3b) causally filtered signal, (Fig. 3c) acausally filtered signal, (Fig. 3d) windowed raw data, and (Fig. 3e) windowed signal with mean removed.

Flux and cumulative flux curves shown in Figure 3 are generally unsatisfying, especially in cases Figure 3a–d. Even though the raw signal (Fig. 3a) possesses decent signal-to-noise, the pressure waveform integration (middle row) reveals a significant nonzero drift, which leads to a nonrealistic (monotonically increasing) flux history. Removal of the drift through application of recursive high-pass digital filters (e.g., 2 pole, 2000 sample, 10 s) leads to additional irreconcilable artifacts. Figure 3b shows causal application of this filter, which exaggerates the signal's rarefactions and leads to a bipolar-shaped flux history. Figure 3c shows a zero-phase filter implementation that leads to a nonphysical acausal pressure rarefaction, which distorts the flux history to an even greater extent.

Table 1
(Event Statistics)—Summary Statistics of the Ten Events Featured in Figures 1 and 5 Ordered Chronologically

Numbers (Small, Medium, Large)	Event Date/Time (mm/dd hh:mm:ss)	SNR	Window Length (s)	Peak-to-Peak Amplitude (Pa)	Maximum Flux (Mm^3/s)	Cumulative Flux (Mm^3)	Maximum Radius (m)	Maximum Volume (Mm^3)
I (S)	07/19 11:19:03	7×10^5	13	69	0.4	0.8	73	2.4
II (S)	07/19 11:44:31	2×10^2	8	15	0.1	0.3	54	2
III (L)	07/19 12:04:39	1×10^4	19	108	1.3	8.3	158	23.1
IV (S)	07/19 18:52:13	2×10^1	7	4	0.04	0.2	44	1
V (L)	07/19 19:50:40	1×10^6	20	206	1.8	8.4	159	28.1
VI (M)	07/20 12:11:47	2×10^4	20	45	0.9	6.9	149	15.5
VII (M)	07/20 16:12:02	8×10^4	20	311	1.6	4.2	126	13.6
VIII (M)	07/21 09:55:47	2×10^5	25	33	0.5	5.2	135	10.8
IX (M)	07/21 11:22:17	1×10^5	9	103	0.8	1.8	94	8.5
X (M)	07/21 14:04:46	7×10^5	20	212	1.4	3.5	118	11.9

Events III and V are considered large, whereas events I, II, and IV are small, and the rest of the events are considered medium-sized. Signal-to-noise ratio (SNR) is calculated as the 10 s variance of signal divided by the 10 s variance of presignal noise. All tabulated parameters, except for maximum volume, are computed from infrasound records. Maximum volume is computed from digitized images as measured in frame number 4 of Figure 6.

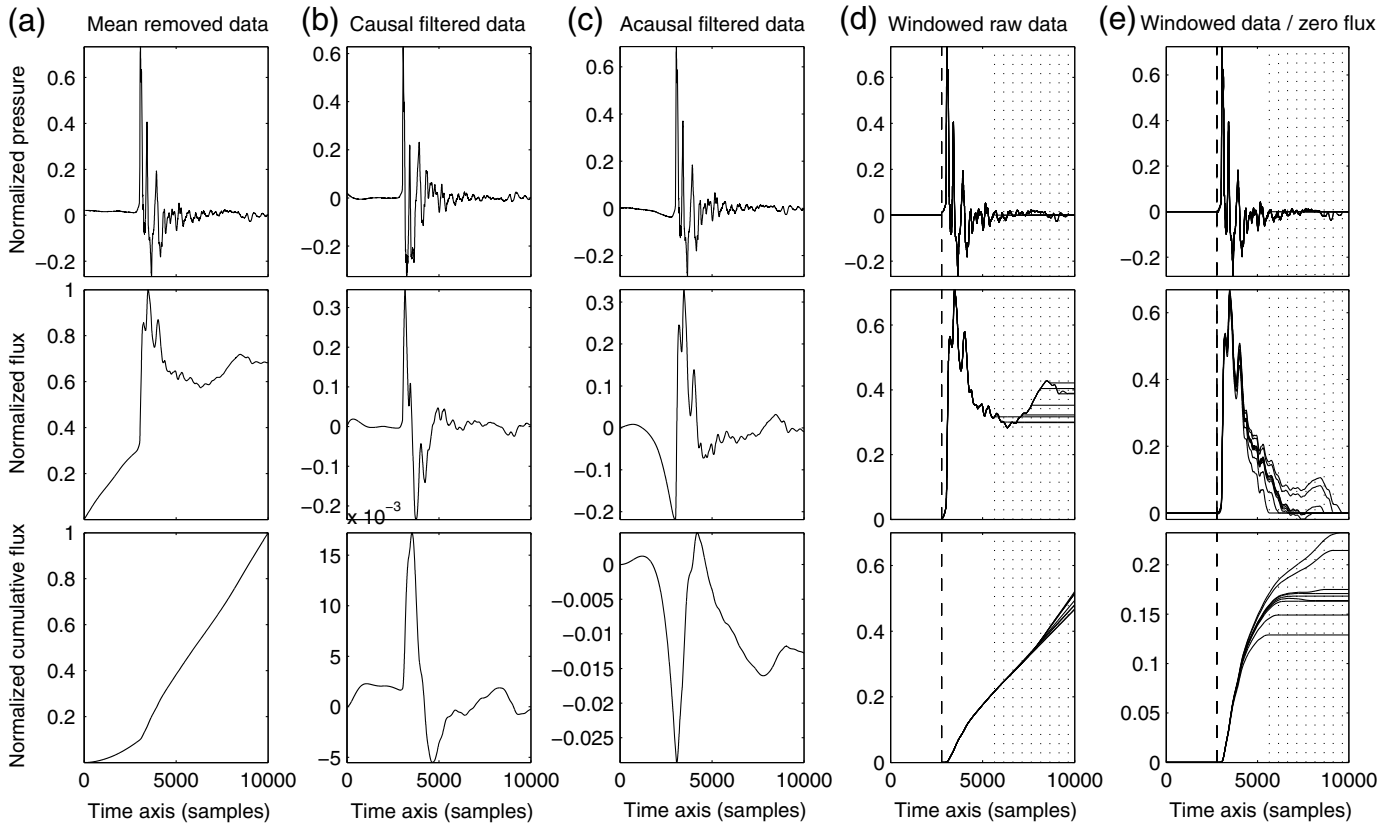

▲ **Figure 3.** Pressure waveforms (top row), integrated waveforms (middle row), and twice integrated waveforms (bottom row) scaled to the normalized amplitudes shown in column A. Example signal III is the event occurring on 19 July at 12:04 (local time) recorded on channel 1 of the KURA array. Time axes are displayed in samples. (a) Normalized raw mean-removed pressure record, (b and c) pressure records following application of a 2 pole, 10 s high-pass filter, (d) same as panel (a), but samples prior to and following the event window have been zeroed. (e) Same as panel (d), but mean has been removed for the duration of the event window (defined by vertical lines). Note that for panels (d) and (e) nine different window end times (solid lines) have been evaluated.

Significantly better results are achieved by windowing the record to the duration of the signal (Fig. 3d,e). Although identification of the end time of the eruption pulse is subjective, it can be facilitated through beamforming techniques when array data is available. Alternatively, the window of primary signal may be manually picked. For many volcano explosions impulsive event onset is easy to identify, but event termination is more difficult to determine as signal tapers gradually toward background levels. Figure 3d indicates scaled flux and cumulative flux for a variety of candidate event end times. Figure 3e shows the same time windows, but the windowed signals have had their mean values removed. These mean-removed windowed waveforms show reasonable flux curves in the sense that calculated flux is forced to begin at zero (prior to the event's onset) and return to zero (after the discrete explosive pulse has presumably ended). Corresponding cumulative flux curves show a ramped time history that asymptotes to a final cumulative outflux. This curve has an intuitively reasonable shape suggesting rapid initial emissions tapering toward diminishing output.

The wide variability in the cumulative outflux values shown in Figure 3e results from uncertainties in identifying the end of the event. A further shortcoming is that mean removal can cause the starting and ending excess pressures (top row of Fig. 3e) to have unrealistic nonzero pressures. Below, we introduce and advocate using a simple signal correction procedure that forces both pressure and flux histories to begin at zero and return to zero after the event terminates. We consider this a justifiable technique for short-duration (tens of seconds or less) explosions that have definitive beginning times. This correction, referred to as finite window zero pressure zero flux (FWZPZF), is enumerated as follows:

1. The beginning time (t_b) and ending time range ($t_e = [t_1, t_2]$) of the high signal-to-noise pressure waveform (i.e., the finite window) are manually identified. Because it is more difficult to identify the end of a signal, which has gradually decreasing amplitude, it is beneficial to test a range of potential signal end times corresponding to a range of candidate event windows.
2. Linear pressure trend lines $\delta p_t(t)$ are calculated corresponding to each of the candidate window ranges. When this trend correction is subtracted from the raw pressure record, that is $\delta p(t) = \delta p_r(t) - \delta p_t(t)$, the conditioned excess pressure waveform must meet the following two criteria:
   - The starting and ending excess pressures must be zero, $\delta p(t_b) = \delta p(t_e) = 0$, such that:

$$\delta p_t(t) = \delta p_r(t_b) + \frac{\delta p_r(t_e) - \delta p_r(t_b)}{t_e - t_b}(t - t_b)$$

   - The integrated pressure (i.e., flux) over the window length must also equal zero, that is:

$$\int_{t_b}^{t_e} \delta p_r dt - \int_{t_b}^{t_e} \delta p_t dt = 0$$

   Because we require the trend line correction $\delta p_t(t)$ to have a constant slope, the second term above is equivalently written as $\int_{t_b}^{t_e} \delta p_t dt = 1/2(t_e - t_b)[\delta p_t(t_b) + \delta p_t(t_e)]$.
   This second criterion implies that the conditioned pressure waveform $\delta p(t)$ must have an associated flux time history that starts and end at zero.
3. It will generally be the case that both criteria can be met for a range of candidate window end values $t_e = \{t_{e1}, t_{e2}, t_{e3}, ..., t_{en}\}$ within the domain $[t_1, t_2]$. In our analysis, an optimal pick for t_e is selected for which the slope of δp_t is minimized:

$$\arg\min\left|\frac{\delta p_t(t_e) - \delta p_t(t_b)}{t_e - t_b}\right|,$$

$$\text{subject to: } t_e \in \{t_{e1}, t_{e2}, t_{e3}, ..., t_{en}\}.$$

   This solution assumes that the pressure trend correction with smallest slope is most reasonable.
4. The conditioned waveform is then calculated as the difference between recorded pressure and trending pressure associated with the lowest slope

$$\delta p(t) = \delta p_r(t) - \delta p_t(t)$$

5. This pressure trace is zero-padded prior to and after the signal window

$$\delta p(t < t_b, t > t_e) = 0$$

6. Flux history $\dot{V}(t)$ is calculated according to equation (2).
7. Cumulative flux history $V(t)$ is calculated according to equation (3).

Figure 4 demonstrates these steps applied to the normalized example pulse of Figure 3 (event III). For this waveform, the candidate window endpoints are sought within the time domain of 5800–8300 samples (a range of 12.5 s). This window is selected by visual examination and corresponds to the time range in which acoustic signal is approximately twice the background level. Transient signal after this time (e.g., at 9000 samples) may include multipath arrivals and/or echoes such as those described in Yokoo *et al.* (2014; this Focus Section).

For the example shown in Figure 4, a total of 54 trend line end times [t_{e1}–t_{e54}] satisfy criteria under step 2, but the trend line t_{e14} with an endpoint at 7422 samples is associated with the smallest absolute slope. Following steps 4 and 5, this trend line is removed from the recorded data, and the signal window is then zero padded. Flux and cumulative flux are then computed from the conditioned pressure trace. It is reassuring that cumulative flux curves diverge only slightly for the 54 trend lines, much less than what is shown in Figure 3e, in which the mean pressure, rather than a trending pressure has been subtracted.

The resultant cumulative volume time history corresponds to volume change over the time scale defined by signal beginning and end. In cases for which only a few seconds of decent signal-to-noise are available, the result will reflect explosive gas emissions over that short time scale. Because noise tends to dominate infrasound records at long periods, the ability to infer total gas flux during long-duration explosions is critically

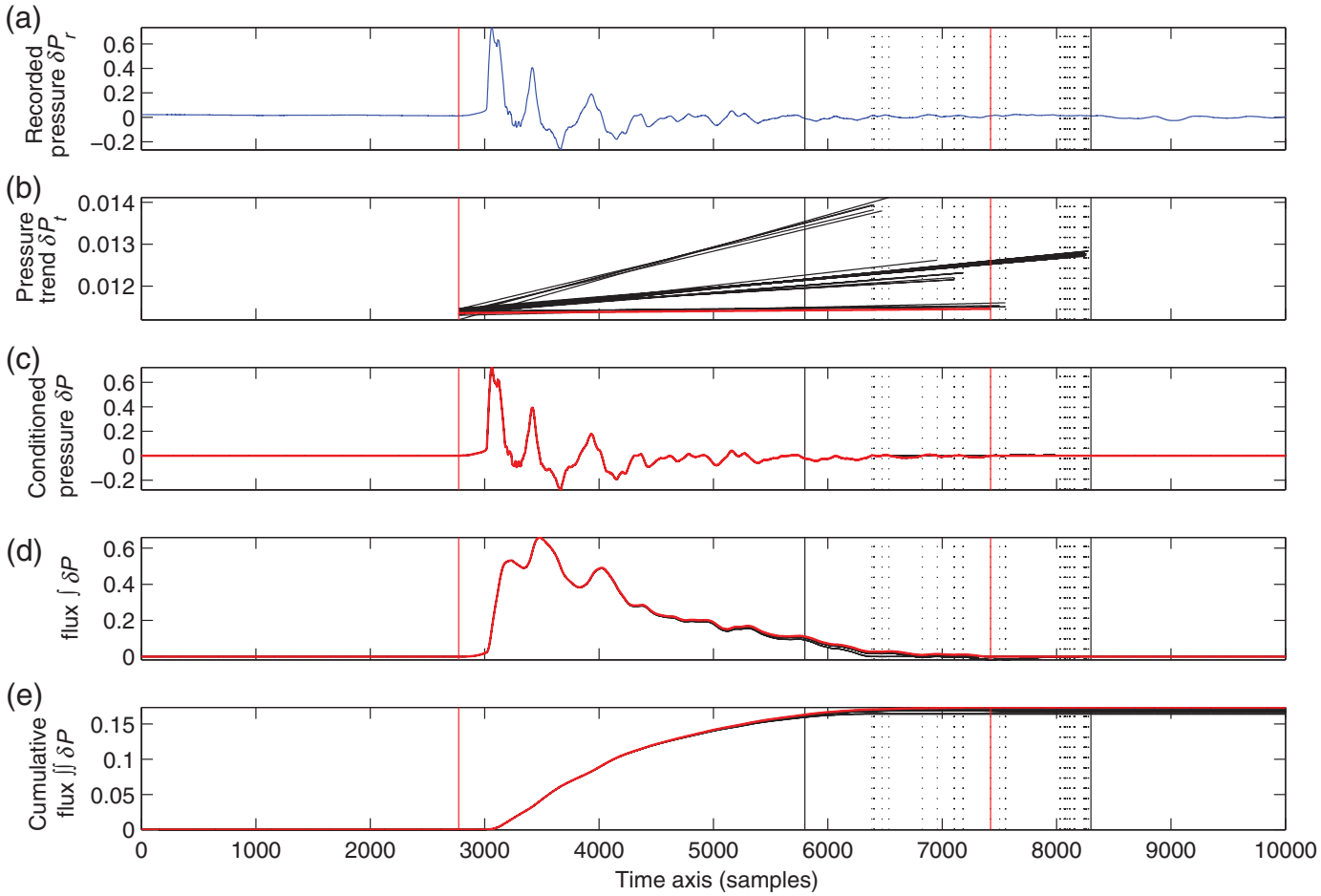

▲ **Figure 4.** Application of the FWZPZF correction to the signal displayed in Figure 3a followed by estimation of flux and cumulative fluxes. (a) Normalized mean-removed waveform recorded on channel 1 of KURA. (b) Candidate trend lines (black) and best slope trend line (red). (c) FWZPZF-corrected signal (indicated for all candidate trend lines). (d) Integrated candidate (black) and best solution (red) normalized flux curves. (e) Double integrated candidate cumulative flux (black) and best solution (red) curves.

limited by the signal-to-noise quality of the recorded long-period signal.

APPLICATION OF THE SIMPLE MONOPOLE SOURCE TO SAKURAJIMA INFRASOUND

We apply the FWZPZF method to 10 Sakurajima explosions occurring between 19 and 21 July. These events compose a subset of the 34 large explosions referenced in Fee *et al.* (2014; this Focus Section), and correspond to those explosions, for which we have recorded coincident high-quality time-lapse imagery at 5.5 s intervals. Analyzed signal comes from four elements of KURA, located ~3500 m from the Showa Crater vent (Fig. 2).

In Figure 5, I–X shows flux and cumulative flux calculations for the ten featured events using multichannel recordings. The initial recordings, pressure trend corrections, and FWZPZF-conditioned waveforms are shown in Figure 5a–c. Duration of the analysis windows, for which signal is clearly above background, ranges between 7 and 25 s for the ten events and is generally longer for the larger amplitude events. Flux histories (Fig. 5d) are calculated from the conditioned pressure records assuming isotropic hemispherical radiation, atmospheric density of ~1 kg/m^3, and a time-of-propagation equal to ~10 s. Cumulative flux (Fig. 5e) shows the inferred time history of the source volume for the duration of the analyzed signal windows. Equivalent source radii (Fig. 5f) are calculated assuming that ejected material perturbs the atmosphere with a hemispherical displacement radius of $R = (3/2\pi V)^{1/3}$. Summary metrics for the ten events are given in Table 1.

It is reassuring that the FWZPZF processing results in a relatively small correction to the raw recorded infrasound. In general, the trend line that is removed has only a small slope or static offset compared to the original signal (Fig. 5b). When the pressure trend line is removed, the calculated flux remains positive, or nearly positive, for the duration of the signal window, implying an outward trending (or expanding) fluid injection, which is intuitively expected during an explosion. It is also noteworthy that the different channels provide cumulative flux values that are similar across the array for a given event; those events for which cumulative flux results vary greatest tend to

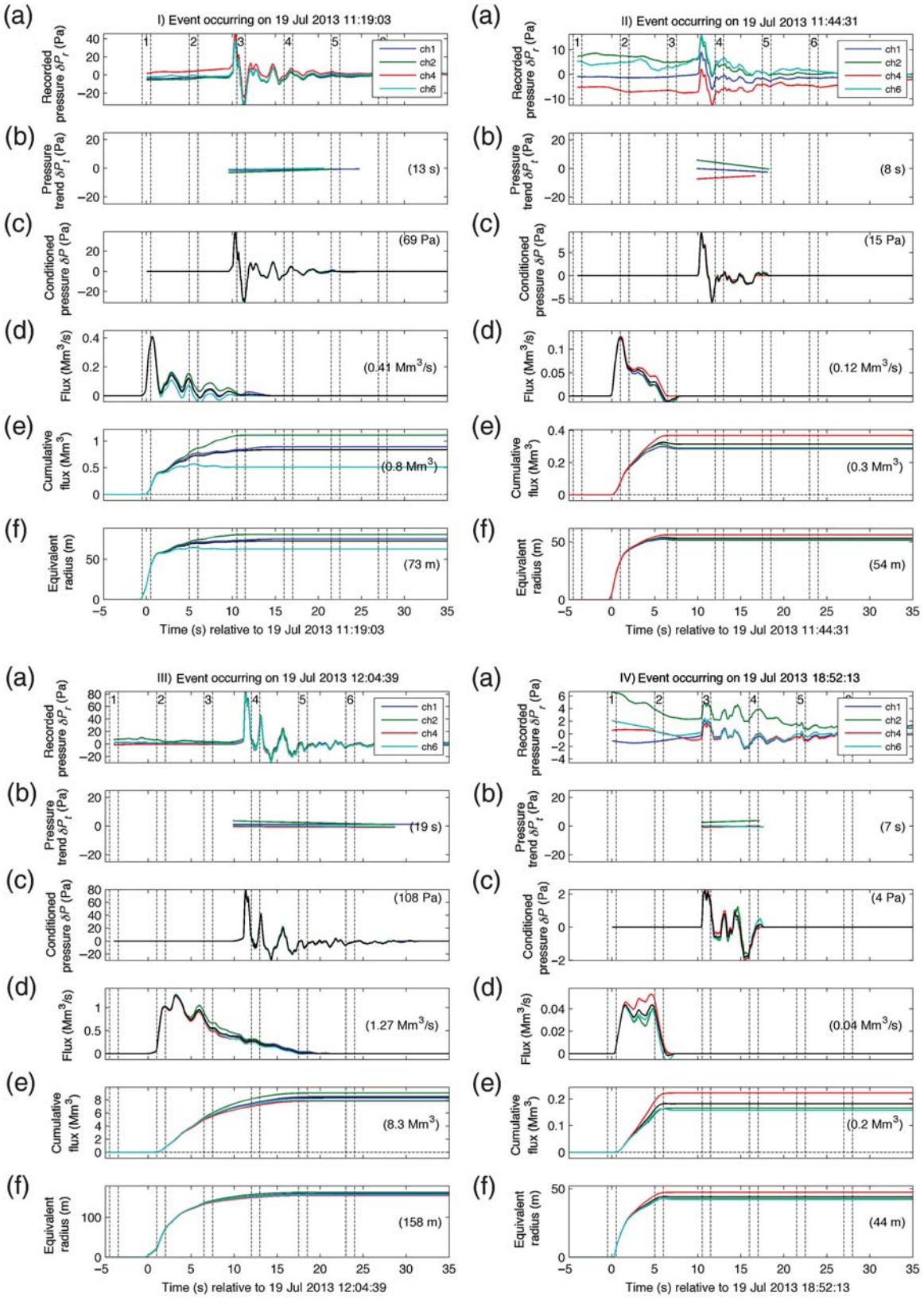

▲ **Figure 5.** (I–X) Application of the FWZPZF correction to the signals displayed in Figure 1, followed by estimation of flux and cumulative fluxes. Unlike the example shown in Figure 4 there has been no amplitude normalization. (a) Mean-removed waveform recorded on channels 1, 2, 4, and 6 of KURA. (b) Best solution trend lines for each channel. (c) FWZPZF-corrected signal for all waveforms that have solutions. (d) Flux curves assuming an atmospheric density of 1 kg/m^3. (e) Cumulative flux curves. Curves in panels (d), (e), and (f) have been time shifted by 10 s to account for infrasound propagation time. (*Continued*)

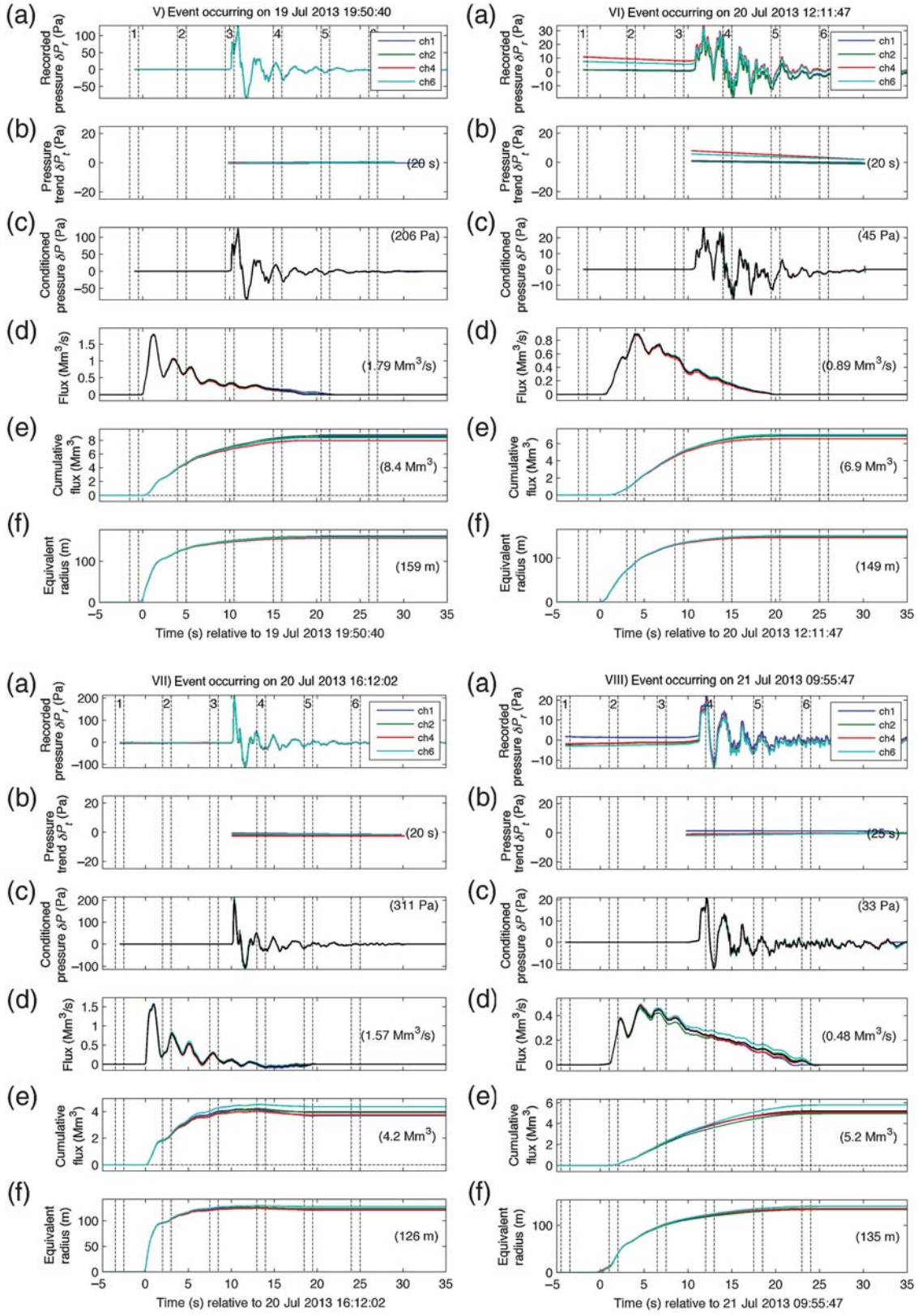

Figure 5. Continued.

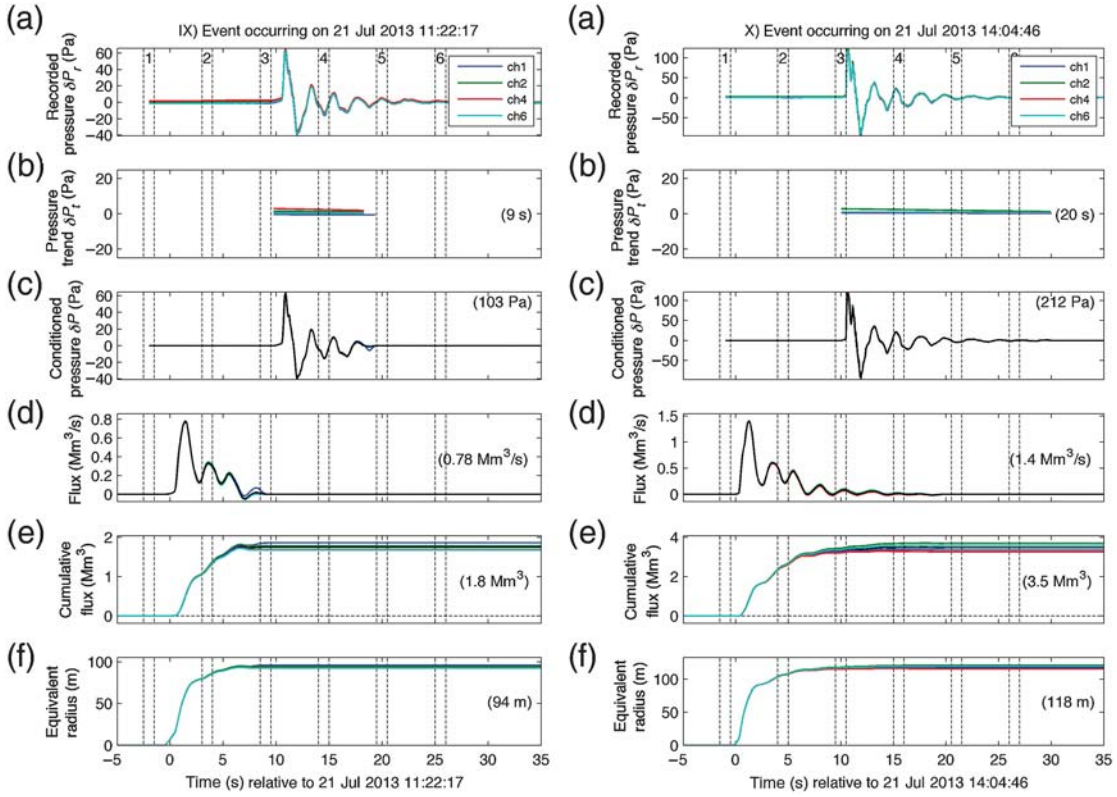

Figure 5. Continued.

correspond to smaller amplitude transients, for which noise influences are relatively larger.

INTERPRETATION OF EXPLOSIVE FLUX HISTORY

Cumulative infrasound-derived volume flux histories compare favorably to plume volumes quantified through examination of time-lapse imagery (Fig. 6). A Canon point-and-shoot camera deployed at KURA was configured to collect images every ~5.5 s using CHDK intervalometer software. The 1600 × 1200 pixel images focused on the Showa Crater, 3.5 km distant, with a zoom set at a 99.2 mm focal length (35 mm equivalent). Diagonal field of view at the distances of Showa was ~1230 m, providing a pixel resolution of 62 cm. Total field of view at this distance was ~1000 m × ~750 m. Timing accuracy was achieved by regularly filming a handheld GPS clock display and is considered accurate to within ±0.5 s.

Expanding plume outlines were manually digitized during the first ~30 s of each initial eruption sequence. Volumes were then calculated from the digitized outlines assuming an axial symmetry in which the plume is composed of a stack of cylindrical disks of thickness dh of 10 m and radius varying with height, that is: $V(t)_{\text{plume}} = \sum_{h=1}^{H} \pi R(t)_h^2 dh$. For at least one explosion (event VIII; July 21 09:55:43), it appears that the initial column comprises dual smaller columns associated with two distinct vents, and for this event we calculated plume volume as $V(t)_{\text{plume}} = \sum_{h=1}^{H} \frac{\pi R(t)_h^2}{2} dh$.

Corresponding cumulative volumes calculated from the infrasound records (Fig. 5) are superimposed as expanding hemispherical shells on the image sequences of Figure 6. Hemispherical profiles were calculated from infrasound-inferred cumulative volumes and have been time shifted to correspond to the source image times (i.e., ~10 s prior to its recording at KURA). Infrasound-inferred volumes and radii (Table 1) provide a convenient means of classifying the Sakurajima eruptions as large (III and V), medium (VI–X), or small (I, II, and IV).

Time evolution of the imagery-derived plume volumes shows a predominantly linear trend out to at least 25 s with maximum volumes for the largest events reaching more than 40 Mm^3 (Fig. 7a). These values are some five times greater than infrasound-derived volumes at 25 s (Fig. 7b). In contrast, infrasound-inferred cumulative volume flux curves show exponentially diminishing outflow, marked by initial rapid ejection of material followed by transition into more gradual fluid outflow. This pattern likely reflects initial explosive expansion driven by intense gas overpressures, followed by slower expansion as the driving pressure diminishes. We infer that beyond about 10 s, continued plume growth, as seen in the time-lapse imagery, is largely driven by buoyant rise of hot gases, which is a steady growth and thus not likely to produce a volumetric source of infrasound. Continuing infrasonic tremor, which can reflect postexplosion open-vent jetting and/or infrasound multipathing off of topography (refer to Yokoo *et al.*, 2014 and Matoza *et al.*, 2014 in this Focus Section), is generally much lower in amplitude than the analyzed explosion pulses.

▲ **Figure 6.** Comparison of plume margin digitization (green) with infrasound-inferred hemispherical volumes and radii (red). Image time interval is ~5.5 s and absolute timing of frames is accurate to ±0.5 s. Frame timing is indicated in Figure 5; parenthetical times (in seconds) correspond to the frame time relative to the explosion onset.

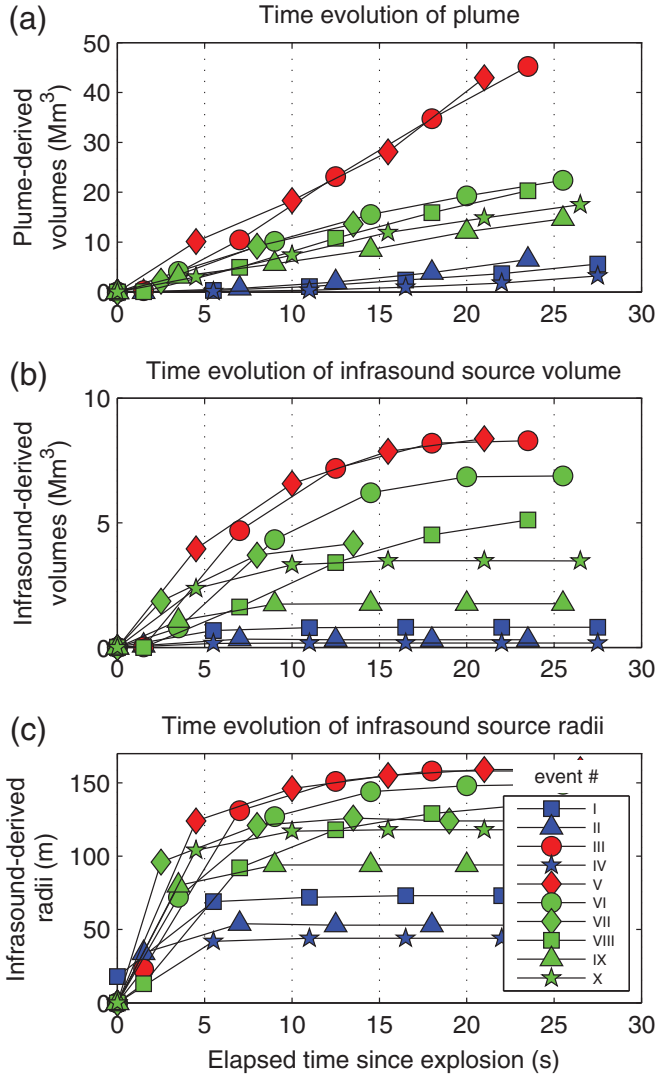

▲ **Figure 7.** Time evolution of (a) the expanding plume volume quantified from time-lapse imagery, (b) infrasound-derived source volumes corresponding to those same time-lapse image times, and (c) corresponding hemispherical radius of assumed hemispherical source. Event numbers are indicated by unique symbols, corresponding to small (blue), medium (green), and large (red) eruptions.

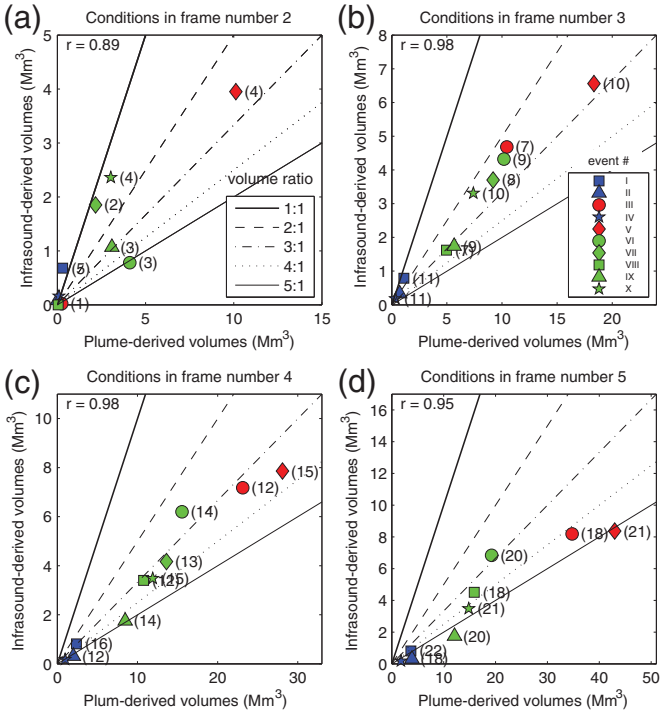

▲ **Figure 8.** Relation between image-derived and infrasound-derived explosive volumes for four distinct time ranges corresponding to (a) second image frame (0–6 s after eruption onset), (b) third image frame (6–11 s after eruption onset), (c) fourth image (11–17 s after eruption onset), and (d) fifth image (17–22 s after eruption onset). Symbol and color scheme is the same as that for Figure 7. Straight lines indicate image-infrasound volume ratios of 1 to 1, 2 to 1, 3 to 1, 4 to 1, and 5 to 1. Parenthetical values indicate time elapsed since eruption onset. Pearson's linear correlation coefficients are indicated as *r* values for each panel.

Comparison of infrasound-inferred volume growth and time-lapse imagery-inferred volume growth is illustrated in Figure 8. Poor correlation is seen in the first few seconds of the eruptive sequence (Fig. 8a) in part because first images correspond to a relatively wide range of times (1–5 s) immediately following the eruption onset. In these early seconds of the eruption, the plume may not even have extended beyond the lip of the crater. As time progresses, however, the infrasound and imagery-derived plume volumes scale much more closely. In particular, the time periods from ~6 to 11 s (Fig. 8b) and 11–17 s (Fig. 8c) show very decent scaling (correlation values of 0.98) between monopole-derived outflux and plume size. It is notable that monopole-inferred volumes are some 2.5 and 3.5 times less than the quantified plume volumes during these two respective time intervals. We attribute this discrepancy to plume volume growth that is noninfrasound producing, either due to continuous venting or buoyant plume expansion. It is notable that by 17–22 s (Fig. 8d) the plume volume is some 5 times greater than the cumulative infrasound-derived volume. At this point the explosive emissions have largely ended even though the column may continue to rise or expand.

Scaling between monopole-derived outflux and plume growth appears satisfactory for the first ~15 s of the gas thrust phase of Sakurajima eruptions. This positive result contrasts with a much poorer correlation between infrasound amplitude and plume-derived volumes (Fig. 9c,d). Interestingly, the two largest amplitude infrasound transients (events VII and X) corresponding to medium-sized volume output events as classified both in plume digitization and in monopole source modeling. This poor scaling between Sakurajima plume height and peak pressure is also noted by Fee *et al.* (2014; this Focus Section) and has been generally observed for explosions at other volcanoes, such as at Tungurahua (Ecuador; Johnson *et al.*, 2005).

It is significant, and notable for monitoring applications, that monopole source modeling over a few tens of seconds better predicts vulcanian plume growth than peak infrasound amplitude.

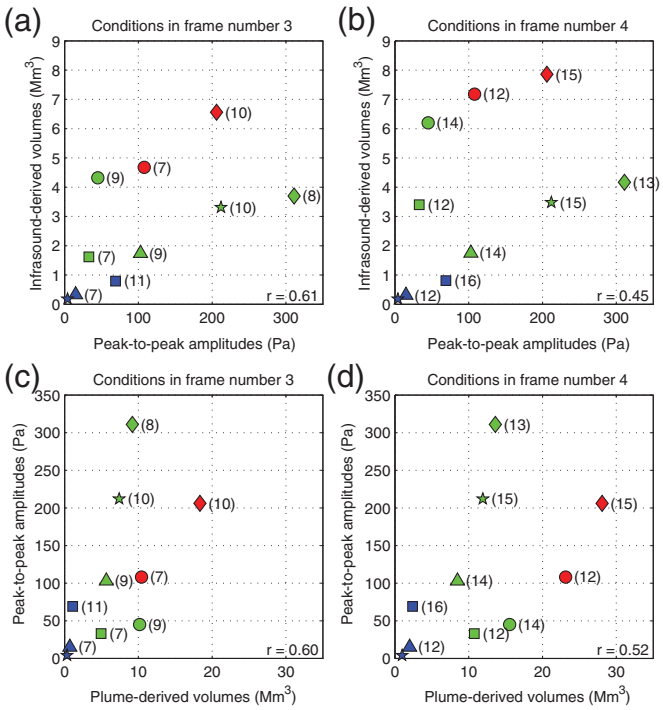

▲ **Figure 9.** Comparison of infrasound peak-to-peak amplitude (as measured at KURA) with (a, b) infrasound inferred cumulative volume fluxes for elapsed times 6–11 s and 11–17 s, and with (c, d) plume-derived volumes at 6–11 s and 11–17 s, respectively. Parenthetical values indicate elapsed time since eruption onset. Symbol and color scheme is the same as that for Figures 7 and 8. Pearson's linear correlation coefficients are indicated as *r* values for each panel.

The two events with largest infrasound-derived cumulative volume fluxes are events III and V. They possess moderately high and very high amplitudes, respectively, but even more significantly, they maintain elevated flux time histories for longer periods. Although equation (1) relates volume acceleration to pressure amplitude, the total flux depends largely upon the time duration of sustained excess pressure. Our results confirm that both the duration of the infrasonic compressional phase(s), as well as peak amplitudes, play contributing roles in determining the initial size of an expanding eruption column. Our findings also explain the relatively scattered correlation between peak-to-peak pressure and monopole-inferred volume outflux (Fig. 9a,b). We conclude that peak infrasound amplitude on its own does not provide enough information to quantify the intensity of a volcanic eruption.

DISCUSSION: CAVEATS

Several assumptions inherent in the presented results merit more detailed attention. Discussion of these source, propagation, and instrument effects on the monopole source model are warranted, but a detailed analysis is beyond the scope of the present paper. Briefly, we summarize several potential sources of error for the presented monopole analyses that deserve future consideration.

Source Considerations

Firstly, our assumption that the Sakurajima infrasound source can be represented by a compact monopole may be disputed. Our modeling suggests that for some events the infrasound-inferred volumes expand to hemispherical dimensions as large as 150 m in radius. Coincident imagery confirms that Sakurajima plume growth (Fig. 6) expands to widths and heights of many hundreds of meters. Assuming that this entire volume is capable of exciting acoustic waves the infrasound source is no longer compact in a strict sense. Dowling (1998) provides an analytical solution for the distant sound field in the case of a noncompact baffled piston of radius a where radiated sound destructively combines at angles oblique to the piston axis. For example, perpendicular to the piston axis a first nodal zero is found for frequency $f = 0.61(c/a)$ (Dowling, 1998; equation 101). Given a large 150 m radius circular piston source this implies total cancellation of sound energy at ~1.4 Hz. Comparable signal diminution might similarly be expected for in-phase hemispherical expansion of a spatially extensive volumetric source. Although the Sakurajima signals have peak energy at ~0.4 Hz (Fig. 1) some higher frequency Sakurajima tones have likely been attenuated considering source dimensions of $\sim 10^2$ m.

Previous studies, including those modeling infrasound radiation from earthquakes (e.g., Arrowsmith *et al.*, 2012), have suggested that some volcano sources may be large with respect to their radiated infrasound wavelengths (Fee and Matoza, 2013). In the case of a distributed volumetric source extended over an uplifting dome surface, the Rayleigh integral has been used to model Santiaguito (Guatemala) volcano infrasound more realistically (Johnson and Lees, 2010). Further analysis is warranted for studying sound genesis of an expanding plume, which could conceivably excite acoustic waves over an expansive region.

This study also neglects the potential role of nonvolumetric acoustic source contributions. Although the monopole source is postulated as a suitable approximation for purely explosive transients, higher order dipole and quadrupole acoustic sources (Woulff and McGetchin, 1976; Johnson *et al.*, 2008; Kim *et al.*, 2012) and jet noise (Matoza *et al.*, 2009; Taddeucci *et al.*, 2014) have been proposed for a range of volcanic eruptive activities. Both jet noise and dipole type sources radiate sound less efficiently than a monopole source (for given eruption energetics) and are thought to radiate sound with an axisymmetric symmetry (Dowling, 1998). Jet noise is also associated with noncompact source regions extending from the vent and up through a collimated jet (Taddeucci *et al.*, 2014). Although Johnson *et al.* (2008) found the dipole acoustic component to be minor compared to the monopole component for strombolian explosions at Erebus, other eruptions, such as those of Sakurajima, may reflect more complex volumetric and nonvolumetric contributions (Matoza *et al.*, 2014; this Focus Section). Matoza *et al.* (2014; this Focus Section) found that jetting signal often comprises a relatively small component of the Sakurajima explosion records in terms of signal amplitude, but that this jetting signal can dominate in the coda. Such jetting signal may

indicate a non-negligible eruption flux, which has not been considered in the present study.

In addition to acoustic source size and mechanistic influences, the degree to which nonlinear near-vent accelerations, which perturb the atmosphere at velocities close to, or exceeding, local sound speed, is an important consideration. Taddeucci *et al.* (2012) identify supersonic emissions for small sized Stromboli (Italy) explosions, which cause the atmosphere to respond with shock wave generation. At Sakurajima shock waves are commonly seen in video records in conjunction with the largest of the recorded infrasound transients (Akihiko Yokoo, Aso Volcanological Laboratory, personal comm., 2013). In general, shocks will decay nonlinearly (and pressure will decrease more rapidly than $1/r$) within a near-vent region until reaching some elastic radius where sound is further propagated as an acoustic wave. For intense eruptions, it is important to recall that recorded infrasound reflects the distension of the atmosphere at some elastic radius and that the original source time volume outflux may be larger than this quantity. This may partially explain the underestimated plume volumes of Sakurajima eruptions in the early seconds of the featured explosions.

Propagation Considerations

In the presented analysis, we have assumed multipathing arrivals to be inconsequential and have also generally neglected topographic or propagation influences and site response. Although these influences are routinely considered for seismic waveform modeling, they are often disregarded during analyses of local infrasound recordings in volcano studies. At local distances atmospheric structure is frequently assumed to be homogeneous, and recorded signal is often considered to be a geometrically scaled version of the pressure time series at the source. Near-sensor topography and free surface effects are often neglected.

At Sakurajima, reflections and kilometer-scale acoustic multipathing have been identified by Yokoo *et al.* (2014; this Focus Section), who analyzed the trailing coda of the Sakurajima explosions out to ~120 s. Using an array of sensors they were able to attribute much of the postexplosion signal to multipathing from echoes off topography, including reflections of the Aira Caldera wall as far as 20 km distant. They also noted that the amplitudes of the indirect arrivals were much smaller than those of the direct energy. In fact, for the explosions shown in the scale of Figure 1, these coda signals are not even visually evident; for this reason, we consider their influence to be negligible.

Near-vent volcano topography likely influences the character of the explosion pulses that are recorded around Sakurajima Island and may be of greater concern. Waveform variability across an infrasound network was highlighted by Fee *et al.* (2014; this Focus Section), who state that waveform shape is affected by intervening topography, which diffracts sound waves around the crater rim and also above and over the edifice. Primary effects of topography are investigated with finite difference time domain techniques such as those presented by Kim *et al.* (2014; this Focus Section), who found that topography influences waveform character most significantly at stations beyond the line-of-sight of the Showa Crater. Other studies, such as those at Tungurahua (Ecuador) by Kim *et al.* (2012), suggest that crater topography near to the vent can induce an asymmetric acoustic radiation pattern that explains the variable sound intensities recorded on the infrasound network there. Because KURA is located relatively proximally and with line-of-sight to the Showa Crater (see profile in Fig. 2) we feel that the waveform is reasonably representative of the source time function. Future work might examine signal from other stations, invert for responsible source time functions and then compute volume fluxes amongst a network of infrasound stations.

Instrument Considerations

As with seismic recordings, infrasound records provide a filtered version of the actual pressure time history of the atmosphere. All infrasonic microphones act as high-pass filters that distort the atmospheric pressure time history in both amplitude and phase. These distortions may appear insignificant for the pressure waveform, but single and double integration enhances the lower frequency artifacts dramatically. If these lower frequencies are not suitably recorded, or if an instrument response correction has not been adequately applied to the infrasound data, corresponding flux and cumulative flux records will be significantly impacted.

For the examples presented herein the signals were recorded with infraBSU instruments possessing a well-characterized response with a single pole corner frequency of ~0.04 Hz. Although no instrument correction was applied to the infraBSU sensors, their corner was considered to be far below that of the primary signal content of Sakurajima infrasound. It is notable, however, that some of the sensors deployed by other teams at Sakurajima varied in their response and/or had an approximate ~0.1 Hz high-pass filter applied during routine processing (see fig. 2 of Fee *et al.*, 2014; this Focus Section). Records from these sensors would require proper signal reconstitution prior to quantification of flux and or volume flux measurements.

CONCLUSION

Sakurajima Volcano is notable for its frequent vulcanian explosions and high-amplitude infrasound pulses, which are large compared with many other episodically erupting volcanoes worldwide (Johnson *et al.*, 2004). As such, Sakurajima provides an exceptional laboratory to explore the relationship between radiated infrasound and material emissions from the vent and to test the suitability of the monopole source model. We have introduced a simple signal conditioning methodology to enable recorded pressure waveforms to be used for flux and cumulative calculations over a few tens of seconds. For a suite of ten explosions occurring during 19–21 July 2013 peak-to-peak amplitudes range from 4 to 300 Pa and infrasound-inferred cumulative fluxes range from 0.2 to 8 Mm^3. We find that the infrasound-inferred cumulative volume fluxes scale very well with imagery-derived measurements of the expanding plume

even though the plume volume is underestimated by a factor of two or three. This systematic volume discrepancy is likely due to plume growth contributions resulting from steady state degassing and/or thermally driven plume growth. We also note a poor correlation between infrasound pressure amplitude and plume volume in the first ten seconds. These results intimate that the trailing infrasound signal beyond the first compressive pulse is fundamentally important to quantify total explosive emissions. Our study offers compelling evidence that infrasound waveform modeling can be used to remotely quantify explosive flux from vulcanian eruptions.

ACKNOWLEDGMENTS

This work was made possible with financial support from National Science Foundation Division of Earth Sciences Grant 1151662, field assistance from students P. Demonte, B. Terbush, and instrument development by T. Ronan and O. Bigelow. We particularly thank Akihiko Yokoo and the Sakurajima Volcano Observatory for logistical assistance and permissions. All raw data presented in this study is provided as a community resource and may be downloaded from the Incorporated Research Institutions for Seismology Data Management Center (IRIS-DMC; Fee *et al.*, 2014; this Focus Section).

REFERENCES

Arrowsmith, S., R. Burlacu, K. Pankow, B. Stump, R. Stead, R. Whitaker, and C. Hayward (2012). A seismoacoustic study of the 2011 January 3 Circleville earthquake, *Geophys. J. Int.* **189,** 1148–1158.

Banister, J. R. (1984). Pressure wave generated by the Mount St. Helens eruption, *J. Geophys. Res.* **89,** 4895–4904.

Bowman, J. R., G. E. Baker, and M. Bahavar (2005). Ambient infrasound noise, *Geophys. Res. Lett.* **32,** doi: 10.1029/2005gl022486.

Dowling, A. P. (1998). Steady-state radiation from sources, in *Handbook of Acoustics* M. Crocker (Editor), John Wiley & Sons, New York, 99–117.

Fee, D., and R. S. Matoza (2013). An overview of volcano infrasound: From hawaiian to plinian, local to global, *J. Volcanol. Geoth. Res.* **249,** 123–139.

Fee, D., A. Yokoo, and J. B. Johnson (2014). Introduction to an open community infrasound dataset from the actively erupting Sakurajima Volcano, Japan, *Seismol. Res. Lett.*, **85,** no. 6, doi: 10.1785/0220140051.

Firstov, P. P., and N. M. Kravchenko (1996). Estimation of the amount of explosive gas released in volcanic eruptions using air waves, *Volcanol. Seismol.* **17,** 547–560.

Gerst, A., M. Hort, R. C. Aster, and J. B. Johnson (2013). The first second of volcanic eruptions from the Erebus Volcano lava lake, Antarctica - Energies, pressures, seismology, and infrasound, *J. Geophys. Res.* **118,** 1–23.

Johnson, J. B. (2003). Generation and propagation of infrasonic airwaves from volcanic explosions, *J. Volcanol. Geoth. Res.* **121,** 1–14.

Johnson, J. B., and J. M. Lees (2010). Sound produced by the rapidly inflating Santiaguito lava dome, Guatemala, *Geophys. Res. Lett.* **37,** doi: 10.1029/2010GL045217.

Johnson, J. B., R. C. Aster, and P. R. Kyle (2004). Volcanic eruptions observed with infrasound, *Geophys. Res. Lett.* **31,** doi: 10.1029/2004gl020020.

Johnson, J. B., R. Aster, K. Jones, P. Kyle, and W. McIntosh (2008). Acoustic source characterization of impulsive strombolian eruptions from the Mount Erebus Lava Lake, *J. Volc. Geoth. Res.* **177,** 673–686.

Johnson, J. B., M. C. Ruiz, J. M. Lees, and P. Ramon (2005). Poor scaling between elastic energy release and eruption intensity at Tungurahua Volcano, Ecuador, *Geophys. Res. Lett.* **32,** L15304, doi: 10.1029/2005GL022847.

Kim, K., and J. M. Lees (2014). Local volcano infrasound and source localization investigated by 3D simulation, *Seismol. Res. Lett.* **85,** no. 6, doi: 10.1785/0220140029.

Kim, K., J. M. Lees, and M. Ruiz (2012). Acoustic multipole source model for volcanic explosions and inversion for source parameters, *Geophys. J. Int.* **191,** 1192–1204.

Kitov, I., J. R. Murphy, O. P. Kusnetsov, B. W. Barker, and N. I. Nedoshivin (1997). An analysis of seismic and acoustic signals measured from a series of atmopsheric and near-surface explosions, *Bull. Seismol. Soc. Am.* **87,** 1553–1562.

Lighthill, M. J. (1978). *Waves in Fluids*, Cambridge University Press, New York.

Marcillo, O., J. B. Johnson, and D. Hart (2012). Implementation, characterization, and evaluation of an inexpensive low-power low-noise infrasound sensor based on a micro-machined differential pressure transducer and a mechanical filter, *J. Atmos. Ocean. Technol.* **29,** 1275–1284.

Matoza, R., D. Fee, M. Garces, J. M. Seiner, P. A. Ramon, and M. A. H. Hedlin (2009). Infrasonic jet noise from volcanic eruptions, *Geophys. Res. Lett.* **36,** doi: 10.1029/2008GL036486.

Matoza, R. S., D. Fee, and T. Lopez (2014). Acoustic characterization of explosion complexity at Sakurajima, Karymsky, and Tungurahua Volcanoes, *Seismol. Res. Lett.* **85,** no. 6, doi: 10.1785/0220140110.

Matoza, R. S., M. Landes, A. Le Pichon, L. Ceranna, and D. Brown (2013). Coherent ambient infrasound recorded by the International Monitoring System, *Geophys. Res. Lett.* **40,** 429–433.

Morrissey, M. M., and B. A. Chouet (1997). Burst conditions of explosive volcanic eruptions recorded on microbaragraphs, *Science* **275,** 1290–1293.

Taddeucci, J., P. Scarlato, A. Capponi, E. Del Bello, C. Cimarelli, D. M. Palladino, and U. Kueppers (2012). High-speed imaging of strombolian explosions: The ejection velocity of pyroclasts, *Geophys. Res. Lett.* **39,** doi: 10.1029/2011GL050404.

Taddeucci, J., J. Sesterhenn, P. Scarlato, K. Stampka, E. Del Bello, J. J. Pena Fernandez, and D. Gaudin (2014). High-speed imaging, acoustic features, and aeroacoustic computations of jet noise from Strombolian (and Vulcanian) explosions, *Geophys. Res. Lett.* **41,** 3096–3102.

Woulff, G., and T. R. McGetchin (1976). Acoustic noise from volcanoes: Theory and experiment, *Geophys. J. Roy. Astron. Soc.* **45,** 601–616.

Yamasato, H. (1997). Quantitative analysis of pyroclastic flows using infrasonic and seismic data at Unzen volcano, Japan, *J. Phys. Earth* **45,** 397–416.

Yokoo, A., M. Iguchi, T. Tameguri, and K. Yamamoto (2013). Processes prior to outbursts of vulcanian eruption at Showa Crater of Sakurajima Volcano, *Bull. Volcanol. Soc. Japan* **58,** 163–181.

Yokoo, A., Y. J. Suzuki, and M. Iguchi (2014). Dual infrasound sources from a Vulcanian eruption of Sakurajim volcano inferred from cross-array observation, *Seismol. Res. Lett.* **85,** no. 6, doi: 10.1785/0220140047.

Jeffrey B. Johnson
Alex J. C. Miller
Department of Geosciences
Boise State University
1910 University Drive
Boise, Idaho 83725 U.S.A.
jeffreybjohnson@boisestate.edu

Published Online 15 October 2014